Determination of Electric-Field, Magnetic-Field, and Electric-Current Distributions of Infrared Optical Antennas: A Near-Field Optical Vector Network Analyzer

Robert L. Olmon,[1,2,‡] Matthias Rang,[2,†] Peter M. Krenz,[4] Brian A. Lail,[5] Laxmikant V. Saraf,[6]
Glenn D. Boreman,[4] and Markus B. Raschke[2,3,*,‡]

[1]*Department of Electrical Engineering, University of Washington, Seattle, Washington 98195, USA*
[2]*Department of Chemistry, University of Washington, Seattle, Washington 98195, USA*
[3]*Department of Physics, University of Washington, Seattle, Washington 98195, USA*
[4]*Center for Research and Education in Optics and Lasers (CREOL), University of Central Florida, Orlando, Florida 32816, USA*
[5]*Department of Electrical and Computer Engineering, Florida Institute of Technology, Melbourne, Florida 32901, USA*
[6]*Environmental Molecular Sciences Laboratory, Pacific Northwest National Laboratory, Richland, Washington 99352, USA*
(Received 5 April 2010; published 15 October 2010)

In addition to the electric field $E(r)$, the associated magnetic field $H(r)$ and current density $J(r)$ characterize any electromagnetic device, providing insight into antenna coupling and mutual impedance. We demonstrate the optical analogue of the radio frequency vector network analyzer implemented in interferometric homodyne scattering-type scanning near-field optical microscopy for obtaining $E(r)$, $H(r)$, and $J(r)$. The approach is generally applicable and demonstrated for the case of a linear coupled-dipole antenna in the midinfrared spectral region. The determination of the underlying 3D vector electric near-field distribution $E(r)$ with nanometer spatial resolution and full phase and amplitude information is enabled by the design of probe tips with selectivity with respect to $E_\parallel$ and $E_\perp$ fabricated by focused ion-beam milling and nano-chemical-vapor-deposition methods.

Optical antennas provide the ability to control and confine light on the nanoscale with applications including nanofocusing for field-enhanced spectroscopy and microscopy, coupling to surface plasmon polariton waveguides and optical nanocircuits, metamaterials, photodetectors, and thermal and molecular sensors [1–7]. However, optical antenna design with the desired functionality and matched impedance [8–10] has remained challenging compared to the radio frequency (rf) regime due to the lack of discrete circuit elements such as baluns and couplers. Instead, one relies on intrinsic optical transitions defined by free carrier, interband, intraband, and related polariton excitations with their geometric resonances giving rise to a high yet poorly understood sensitivity to these material properties and nanoscopic structural details.

As the primary source term for the optical magnetic $H(r)$ and electric $E(r)$ vector fields of the antenna, the underlying current density distribution $J(r)$ reflects the fundamental electrodynamic interaction and local coupling of antenna elements. While $E(r)$ and the weaker $H(r)$ fields only indirectly reveal the details of their microscopic origin via their spatial distribution, knowledge of the antenna current standing wave can provide a more direct and sensitive insight into impedance distribution, resonant frequency, or the coupling with neighboring antennas [11,12]. Access to the current distribution is thus desired for optical antenna design and coupling to antenna loads, yet even with special nonlinear [13] and THz techniques [14] direct current measurements with high spatial resolution have remained difficult experimentally.

Here we demonstrate the determination of the conduction current density distribution $J(r)$ and its associated magnetic vector field $H(r)$ from measurement of the antenna electric vector field $E(r)$, taking advantage of the vector relationship in free space given by Faraday's Law $H(r) = i/(\omega\mu_0)\nabla \times E(r)$ and Hallén's integral equation relating in-plane $E(r)$ to $J(r)$ [11]. This emphasizes the powerful implication that if $E(r)$ is known with sufficient detail, then all electrodynamic parameters describing the optical response may be deduced. We measure $E(r)$ in the reactive near field with high sensitivity and nanometer spatial resolution by a special implementation of scattering-type scanning near-field optical microscopy (s-SNOM) [see Figs. 1(a) and 1(b)]. We derive $H(r)$ and $J(r)$ from the measured $E(r)$ for an infrared (IR) linear coupled-dipole optical antenna resonant at 28.3 THz ($\lambda = 10.6$ μm), identifying the coupling between the antenna segments from details of the field and current distributions. With the ability to determine $E(r)$, $H(r)$, and $J(r)$ with amplitude and phase with nanometer spatial resolution this work demonstrates the optical analogue of the rf vector network analyzer.

Although optical $H(r)$ can, in principle, be measured directly as shown recently using split-ring resonator probes [15], the weaker Lorentz force associated with the magnetic light-matter interaction, compared to the Coulomb interaction, results in general in a higher detection sensitivity for $E(r)$, from which the associated $H(r)$ field can be derived in free space.

A detailed understanding of optical antennas in the IR in terms of directional response, wavelength selectivity, and
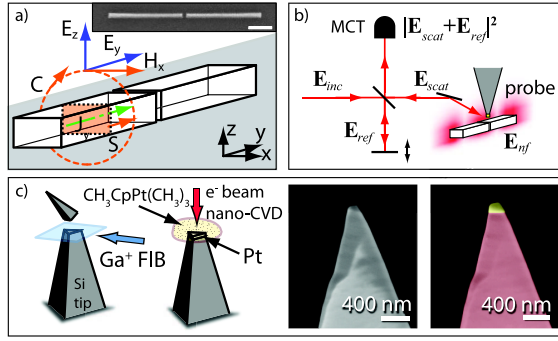
FIG. 1 (color online). Schematic of coupled-dipole antenna geometry (a) with current density $J(y)$ through cross sectional surface S and associated magnetic field $H_x(y, z)$ on contour C related to the measured curl of the electric field $E(y, z)$ in the antenna $y - z$ mirror plane. Inset: SEM image, scale bar 500 nm. (b) Schematic of amplitude-, phase-, and polarization-resolved interferometric homodyne 3D $E(r)$ vector near-field s-SNOM imaging. (c) Pt point dipole probe antenna fabricated on a Si AFM tip by FIB and nano-CVD. SEM images of the tip before (left) and after (right) Pt deposition with Si (red) and Pt (yellow) regions highlighted.

capture cross section is desirable for device applications such as high sensitivity thermal imaging, IR plasmonics, chemical sensing, or direct solar energy conversion. With its mirror symmetry and simple phase behavior, the coupled resonant IR dipole antenna provides a well-defined model system.

Aperture probes [16] and s-SNOM were previously used to study selected electric-field vector components [10,17,18] or near-surface antenna fields [19]. Tip-sample coupling [20] and tip scattering anisotropy [21,22] using nanoparticle functionalized probe tips were found to be critical for measuring the full electric vector near-field distribution $E(r)$. For our generalized approach of vector-resolved detection of $E(r)$ we engineer probe tips with defined polarization response and scattering sensitivity with regard to orthogonal $E_{\parallel}$ and $E_{\perp}$ field components. Following a theoretical design (see supplement [23]), by combining focused ion beam (FIB) milling and electron beam assisted metal-organic chemical vapor deposition (nano-CVD) an off-resonant Pt point dipole probe is fabricated perpendicularly onto the apex of a commercial AFM Si cantilever tip as shown in Fig. 1(c). The normalized tip response to s- and p-polarized light (0.97 and 1.0, respectively) allows the assignment of the relative magnitudes of the in-plane and out-of-plane vector components. A low depolarization scattering, as critical for vector-resolved s-SNOM, is verified experimentally with minimal depolarization of ~1%. Despite the 200 nm size, with the triangular platelet Pt probe oriented under a slight tilt angle of a few degrees with respect to the sample plane, the s-SNOM spatial resolution is found to be dominated by the Pt prism corner dimensions of a few 10's of nm.

The linear Au dimer antenna length of 1.7 μm is chosen to correspond to the primary dipolar resonance with exci-

tation at $\lambda = 10.6$ μm considering the effective wavelength scaling as established previously [24,17,25]. The dipoles are arranged in collinear pairs to form coupled dimers with interantenna gaps of 80 nm.

The general s-SNOM measurement scheme is shown in Fig. 1(b). With the object under far-field excitation of E_{inc} of defined polarization, the tip-scattered near-field signal $E_{\text{scat}} \propto E_{\text{nf}}$ is collected in a collinear backscattering geometry, with interferometric homodyne amplification for amplitude, phase, and polarization-resolved detection [26–28] with $S_{\text{det}} = |E_{\text{scat}} + E_{\text{ref}}|^2$. The IR dipole antennas are excited using a CO_2 laser polarized parallel to the antenna axis, incident at an angle of 60° with respect to the surface normal, using a Cassegrain objective (NA = 0.5) [26,17]. With in-plane polarized excitation ($s = y$ axis), and s and p (z axis) detection, tip-sample coupling is negligible [26,29] and allows for minimally invasive $E(r)$ measurement. With the lock-in amplifier referenced to the second-harmonic of the tip dither frequency for far-field background suppression [27], the signal is related to the intensity gradient of the optical near-field in the z direction [26]. The field amplitude for each field component is then obtained numerically from the integral of the detected field gradient with the integration variable combined into a constant background term.

Figure 2 shows the resulting 2D $E(y, z)$ near-field map in the $x = 0$ plane above the dimer antenna (a) (inset, close-up view). The data are acquired in lift mode with sampling steps of 42 nm $\times$ 2 nm (corresponding to 128 $\times$ 48 pixels) in the y and z directions, respectively. The field vectors at each point indicate the direction and relative amplitude (also given by color code) of $|E_{\text{nf}}| = (E_y^2 + E_z^2)^{1/2}$. For comparison, a simulation with the antennas modeled as Au half cylinders terminated by quarter spheres on a Si substrate is shown (b). Line scans of topography and the two individual field components E_y and E_z at $z = 90$ nm are shown for experiment (c) and theory (d). Three distinct regions of high field magnitude are seen in E_y, corresponding to the locations of high charge concentration associated with the gap region and outer antenna terminals. These three regions oscillate in phase, in contrast to the alternating phase changes of π of the associated E_z field [26,17]. The E_y-dominated gap field is characterized by a large homogeneous field enhancement due to the antenna coupling, with small or zero E_z component due to phase reversal in the gap. The total field $|E_{\text{nf}}|$ at $z = 90$ nm is shown overlaid in Figs. 2(a) and 2(b) (white line). In contrast to earlier studies with unspecified polarization detection [18], it is evident that the global field maximum occurs just outside the gap at the metal edges where the field lines converge associated with the small radius of curvature (see supplement for details [23]).

Recovery of $H(r)$ and $J(r)$.—With the plane wave excitation with wave vector approximately perpendicular to the $y - z$ mirror plane of the coupled-dipole antenna where $E_x = 0$ V/m, the measured 2D distribution of E_y and E_z
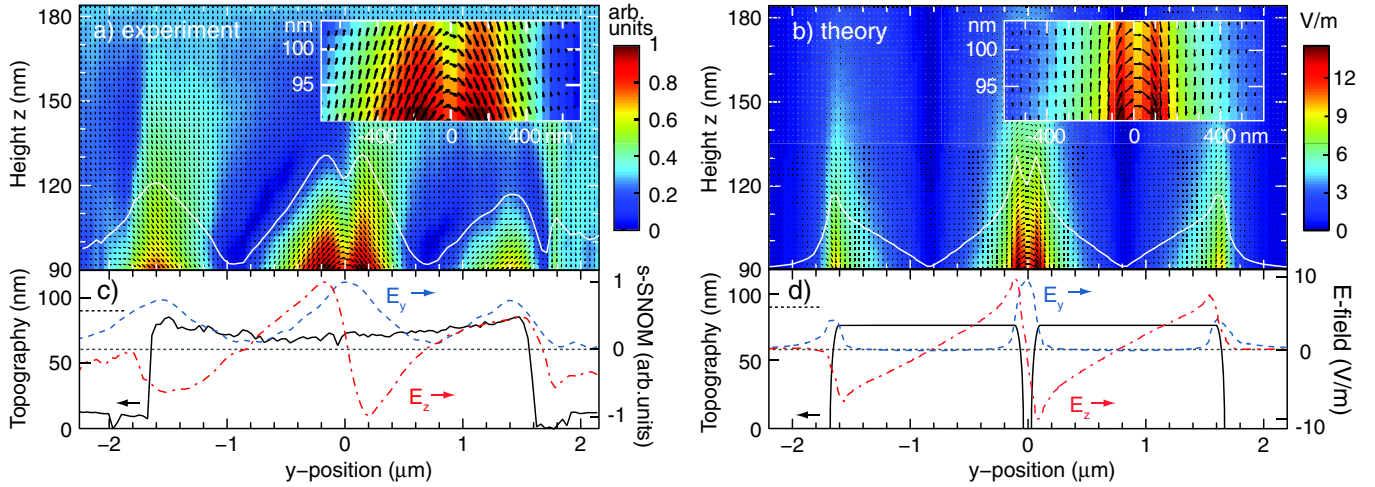
FIG. 2 (color online).   Measured (a),(c) and theoretical (b),(d) near-field vector distribution of linear Au IR optical dimer antenna: (a) $\boldsymbol{E}(y, z)$ in the $y - z$ plane and (b) corresponding theory. Field magnitude is given by vector length and color map. A line scan (white line) for $|\boldsymbol{E}(y, z)|$ at $z = 90$ nm is shown. Inset: Close-up views of the near-field vector distribution near $y = 0$. Line scans (c),(d) show topography and measured E-field components E_y and E_z at $z = 90$ nm above the antenna surface. The 80 nm gap is not fully resolved in topography due to the probe tip size.

is sufficient to fully characterize the antenna response. Applying Faraday's Law the corresponding magnetic field is obtained from the curl of the electric field as $H_x(y, z) = i(\partial E_z/\partial y - \partial E_y/\partial z)/(\omega\mu_0)$ (for procedural details see the supplement [23]). Figure 3(a) shows the resulting $H_x(y, z)$ distribution obtained from the measured $\boldsymbol{E}(y, z)$ field of Fig. 2(a). Comparison with theory (b) shows good agreement with the characteristic near central $H_x(y, z)$ maximum for each dipole, the corresponding minima at the extremities, and the decay length, as seen in the respective line cuts of the magnetic field as a function of

FIG. 3 (color online).   Magnetic field $H_x(y, z)$ above coupled-dipole antennas (position indicated by gray dashed lines) derived from the the electric near-field distribution $\boldsymbol{E}(\boldsymbol{r})$, experiment (a) and theory (b). Horizontal variation of $H_x(y)$ (c) and vertical distance dependence of $H_x(z)$ (d) [black dashed lines in (a) and (b)]. Because of the antenna symmetry, $H_x(y, z)$ in the $y - z$ mirror plane represents the full magnetic antenna response.

lateral position y along the rod axis at height $z = 100$ nm (c), and along z over the center of a single rod (d). The enhanced fluctuations seen in $H_x(y, z)$ compared to the measured $\boldsymbol{E}(y, z)$ emphasize the requirement for accurate and high resolution near-field $\boldsymbol{E}(\boldsymbol{r})$ data, since the magnetic-field determination relies on the difference between orthogonal field gradients, making it very sensitive to noise, systematic errors in the detected signal, and depolarized scattering, especially at the center of each antenna segment, where $\partial E_y/\partial z$ is small.

The underlying one-dimensional average current density distribution $I(y)$ is shown in Fig. 4(a), retrieved in magnitude (red) and corresponding phase ϕ (green) from the experimental $E_y(z = 90$ nm) using the method of moments to solve Hallén's integral equation with a pulse basis and point-matching and with $I = 0$ boundary conditions at the antenna terminals [30]. The result is a two-sided, nearly symmetric current distribution centered on each dipole as expected to first order for this geometry. With the possibility that local field enhancement from the metal surface roughness may distort the fundamental antenna current mode, as an alternative approach, we restrict the analysis to the E-field region within the gap and outside the terminals by masking the field on the metal surface, with the resulting $I(y)$ shown in Fig. 4(b) (for details see supplement [23]). This results in a slightly asymmetric $I(y)$ distribution for each dipole with a discernible peak shift towards the gap. Alternatively, and for comparison, the current derived from the magnetic-field of Fig. 3 using $\boldsymbol{J}(\boldsymbol{r}) = \nabla \times \boldsymbol{H}(\boldsymbol{r})$ is shown in (c). Despite the significant amplification of the noise, a current peak shift is seen. For comparison, Fig. 4(d) shows $I(y)$ derived from the corresponding simulated in-plane near-field distribution. With a current peak shift of approximately 100 nm towards
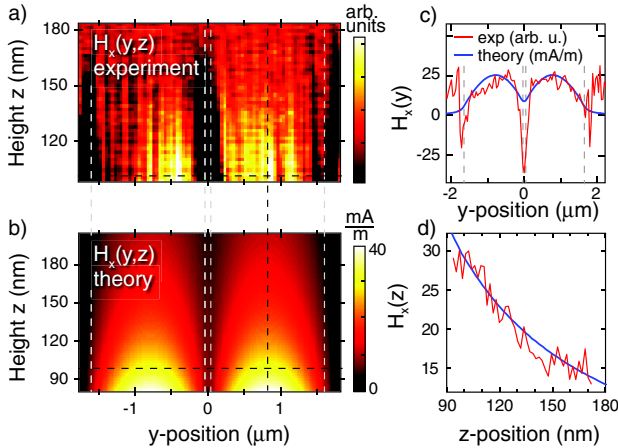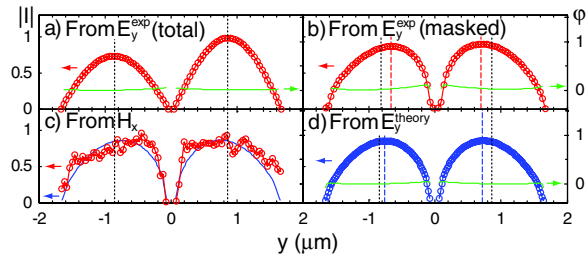
FIG. 4 (color online).   Current distribution $I(y)$ along antenna dimer reconstructed from E_y (a, total and b, masked to remove scattering due to metal roughness) and H_x (c) with normalized amplitude $|I|$ and phase ϕ [radians]. A shift in current maximum (dashed line) of 100–200 nm with respect to geometric center (dotted lines) results from capacitive gap coupling. For comparison, (d) and solid line in (c) show $I(y)$ from theory.

the gap a semiquantitative agreement is found with the experimental results.

The peak shift seen in the current distribution in Figs. 4(b)–4(d) is the result of interdipole antenna coupling associated with Coulomb interaction across the gap and mutual impedance between the antennas. The coupling between antennas in this collinear arrangement is generally weak, in contrast to, e.g., side-by-side parallel arrangement [11,17]. The deviations from theory due to fine structural details, where critical antenna dimensions in the nanometer range are often comparable to fabrication imperfections, have been a long standing concern in optical antenna design, with the effect of altering the desired field characteristics and local field enhancement magnitude. The above result indicates that theory alone is insufficient to predict the full antenna behavior, emphasizing the need for practical characterization techniques for optical antenna design as presented here.

In conventional probing of rf devices, the magnitude and phase of the potential at the input of a scanning probe antenna (typically a small dipole or loop) is measured using a vector network analyzer or a spectrum analyzer with a known reference frequency with the probe acting as the receiver in transmission (S_{21}) mode [31]. In the s-SNOM-based implementation demonstrated here, the combination of the radiating near-field probe tip, the phase coherent excitation source (the laser), and the interferometric homodyne signal detection together comprise the optical analogue of the electronic rf homodyne VNA, as used, e.g., for rf near-field measurements, thus bringing this important technique to the optical regime.

In summary, we developed a nano-optical vector-network analyzer based on s-SNOM as a tool for optical antenna characterization, analysis, and design. For the case of antennas with one mirror symmetry, a single excitation or detection pathway probing of the two near-field components perpendicular to the incident $\boldsymbol{k}$ vector is sufficient for the complete antenna characterization. Generalization of the approach using two orthogonal optical pathways and

measurement of the full relative temporal phase evolution [19] affords vector-resolved detection in three dimensions enabling $\boldsymbol{E}$, $\boldsymbol{H}$, and $\boldsymbol{J}$ measurement for arbitrary optical antenna geometries.

*markus.raschke@colorado.edu
†Present address: Forschungsinstitut am Goetheanum, CH 4143 Dornach, Switzerland.
‡Present address: Department of Physics, and JILA, University of Colorado at Boulder, Colorado 80309, USA.

[1] P. J. Schuck et al., Phys. Rev. Lett. **94**, 017402 (2005).
[2] P. Bharadwaj, B. Deutsch, and L. Novotny, Adv. Opt. Photon. **1**, 438 (2009).
[3] J. N. Farahani et al., Phys. Rev. Lett. **95**, 017402 (2005).
[4] S. Zhang et al., Phys. Rev. Lett. **101**, 047401 (2008).
[5] S. I. Bozhevolnyi and T. Sondergaard, Opt. Express **15**, 10869 (2007).
[6] J. Wenger et al., Opt. Express **16**, 3008 (2008).
[7] J. Alda et al., Nanotechnology **16**, S230 (2005).
[8] L. Tang et al., Nat. Photon. **2**, 226 (2008).
[9] A. Alù and N. Engheta, Phys. Rev. Lett. **101**, 043901 (2008).
[10] M. Schnell et al., Nat. Photon. **3**, 287 (2009).
[11] C. A. Balanis, Antenna Theory: Analysis and Design (Wiley, New York, 1997).
[12] A. Sundaramurthy et al., Phys. Rev. B **72**, 165409 (2005).
[13] J. I. Dadap et al., Opt. Lett. **24**, 1059 (1999).
[14] M. A. Seo et al., Opt. Express **15**, 11781 (2007).
[15] M. Burresi et al., Science **326**, 550 (2009).
[16] M. Burresi et al., Phys. Rev. Lett. **102**, 033902 (2009).
[17] R. L. Olmon et al., Opt. Express **16**, 20295 (2008).
[18] N. Yu et al., Appl. Phys. Lett. **91**, 173113 (2007).
[19] M. Schnell et al., Nano Lett. **10**, 3524 (2010).
[20] L. Novotny and C. Henkel, Opt. Lett. **33**, 1029 (2008).
[21] K. G. Lee et al., Nat. Photon. **1**, 53 (2007).
[22] H. Gersen et al., Nat. Photon. **1**, 242 (2007).
[23] See supplementary material at http://link.aps.org/supplemental/10.1103/PhysRevLett.105.167403 for details regarding vector field probing and calculation of the magnetic field and current.
[24] L. Novotny, Phys. Rev. Lett. **98**, 266802 (2007).
[25] F. Neubrech et al., Appl. Phys. Lett. **89**, 253104 (2006).
[26] A. C. Jones et al., Nano Lett. **9**, 2553 (2009).
[27] F. Keilmann and R. Hillenbrand, Phil. Trans. R. Soc. A **362**, 787 (2004).
[28] A. Bek, R. Vogelgesang, and K. Kern, Rev. Sci. Instrum. **77**, 043703 (2006).
[29] R. Esteban et al., Nano Lett. **8**, 3155 (2008).
[30] S. J. Orfanidis, Electromagnetic Waves and Antennas (http://www.ece.rutgers.edu/~orfanidi/ewa/, 2008).
[31] D. Baudry et al., IEEE Trans Electromag. Compat. **49**, 485 (2007).